Article

Control of Wave Energy Converters with Discrete Displacement Hydraulic Power Take-Off Units

Shangyan Zou [1]*, Ossama Abdelkhalik [1]

[1] Department of Mechianical Engineering, Michigan Technological University, 1400 Townsend Dr, Houghton, MI 49931, USA; ooabdelk@mtu.edu
* Correspondence: szou2@mtu.edu

Academic Editor: name
Version February 7, 2018 submitted to J. Mar. Sci. Eng.; Typeset by LaTeX using class file mdpi.cls

Abstract: The control of an ocean WEC (WEC) impacts the harvested energy. Several control methods have been developed over the past few decades that aim to maximize the harvested energy. Many of these methods were developed based on an unconstrained dynamic model assuming an ideal PTO (PTO) unit. This study presents numerical tests and comparisons of few recently developed control methods. The testing is conducted using a numerical simulator that simulates a hydraulic PTO. The PTO imposes constraints on the maximum attainable control force and maximum stroke. In addition, a PTO has its own dynamics which may impact the performance of some control strategies.

Keywords: Wave Energy Conversion; PTO Units; Hydraulic PTO; WEC control

1. Introduction and Background

The control of ocean WECs (WECs) have received a great deal of interest over the past several decades. In recent years in particular there has been significant developments on maximizing the harvested energy from WECs from a control system analysis and design perspective. Many of these control methods were proposed for the idealistic case in the absence of stroke or force limitations, and assuming ideal PTO (PTO) units. This paper presents comparisons between some of the recently developed control methods; these simulations include a model for a hydraulic PTO, and consequently it imposes constraints on the displacement of the buoy and on the maximum possible control force. These simulations also highlight some insight regarding the needed reactive power for some of the discussed control methods. Several earlier controllers were developed in [1–3] for WECs with hydraulic PTOs. A hydraulic system was validated using AMEsim in [4]. The control methods discussed in this paper are being tested using hydraulic PTOs for the first time in this paper.

This section presents a review for hydraulic PTO units. Fig. 1 is a general layout for a typical hydraulic PTO. The hydraulic system is composed by the actuator, the valve, the accumulators and the motor. The motion of the buoy will compress/decompress the chamber of the actuator and transfer the wave power to the hydraulic system. All the hydraulic systems can be mainly categorized into three groups: the constant pressure, the variable pressure, and the constant-variable pressure hydraulic systems [5,6].

1.1. Constant pressure configuration

The first configuration is constructed with a low pressure accumulator and a high pressure accumulator. This type of hydraulic system can be achieved with a simple mechanism, and the control level is low.

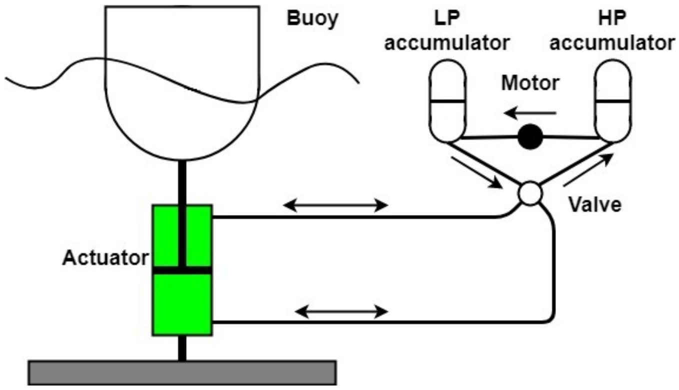

Figure 1. General layout for a hydraulic PTO

The typical configuration of a constant pressure hydraulic system is presented in detail in [7,8], using phase control. Control of the constant pressure hydraulic system is achieved by implementing auxiliary accumulators in [3]. The latching and declutching controls are demonstrated in [9] using a constant pressure hydraulic system. Additionally, a declutching control is presented in [10] for controlling a hydraulic PTO with switching on and off using a by-pass valve. The method is also tested with the SEAREV WEC with an even higher energy absorption. A detail of a single acting hydraulic PTO system with the phase control is presented in [11,12]. The hydraulic system implemented in SEAREV is presented in [13]. In reference [14], a novel model of the hydraulic PTO of the Pelamis WEC is developed that has the ability to apply reactive power for impedance matching. In reference [15], a double action WEC of an inverse pendulum is proposed. Reference [15] found that a double action PTO can supply the output power in each wave period without a large instantaneous fluctuating power. A double-acting hydraulic cylinder array is developed in [16], where the model is found to be adaptive to different sea states to achieve higher energy extraction. Reference [17] presents the optimization of a WEC hydraulic PTO for an irregular wave where the optimal damping is achieved by altering the displacement of the variable displacement hydraulic motor. Reference [18] presents a design and the testing of a hybrid WEC that obtains a higher energy absorption than a single oscillating body with a hydraulic PTO. A discrete displacement hydraulic PTO system is studied in [19] for the Wavestar WEC. An energy conversion efficiency of 70% was achieved. Additionally, adjusting of the force applied by the PTO is accomplished through implementing multiple chambers.

1.2. Variable pressure

The variable pressure hydraulic system is suggested in [20–22]. In this situation, the piston is connected directly to a hydraulic motor. This system can achieve better controllability, but the fluctuation of the output power is not negligible. Two hydraulic PTO systems are compared in [23], where a constant pressure hydraulic PTO and a variable pressure hydraulic PTO systems are compared. It was shown that a variable pressure hydraulic PTO system would have a higher efficiency. The variable pressure approach was also investigated in [24], where the hydraulic motor is used in order to remove the accumulator and control the output using the generator directly. A comparison between a constant pressure system and a variable pressure system was conducted in [25]; validation was conducted using the AMEsim and demonstrated a good agreement. Power smoothing was achieved in [26] by means of an energy storage.

1.3. Variable - Constant pressure

The Variable - Constant pressure hydraulic system is constructed with two parts: the variable pressure part and the constant pressure part. The variable pressure part is accomplished by a hydraulic transformer. A generic oil-hydraulic PTO system, applied to different WECs, is introduced in [27]. In reference [28], a PID controller is developed and the reactive power is supplied by the hydraulic transformer (working as a Pump). A suboptimal control was suggested in [28] for practical implementation in terms of the efficiency of the PTO.

2. The WEC dynamics

In this section, the WEC dynamic model used in this paper is briefed. In this paper, the floater used in the simulations is the Wavestar absorber [9]. The floater has a single degree of freedom motion which is the pitch rotation. The geometry of the proposed absorber is depicted in Fig. 2.

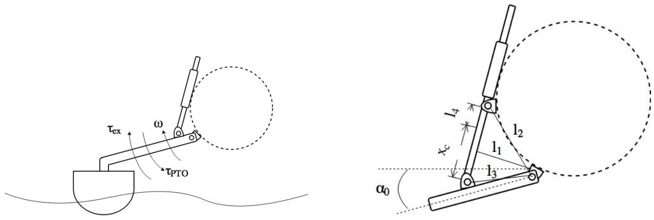

Figure 2. The geometry of the Wavestar absorber

The WEC dynamic model can be described based on linear wave theory as:

$$J_{rigid}\ddot{\theta} = \tau_{ex} + \tau_{res} + \tau_{rad} - \tau_G - \tau_{PTO} \tag{1}$$

where J_{rigid} is the moment of inertia of the rigid body. θ is the pitch rotation of the floater. τ_{ex} is the wave excitation torque acting on the buoy, τ_{res} is the restoring momentum, τ_{rad} is the radiation torque, and τ_G is the torque caused by the gravity. The PTO torque is τ_{PTO} which is applied by the hydraulic cylinder. The equation of motion can be further expanded as:

$$\ddot{\theta} = \frac{1}{J_{rigid} + J_\infty}(\tau_{ex} - \tau_{PTO} - K_{res}\theta - h_r * \dot{\theta}) \tag{2}$$

where J_∞ is the moment of the added mass at infinite frequency, K_{res} is the coefficient of the hydro-static restoring torque, and h_r is the radiation impulse response function. In Eq. (2), the radiation torque is expanded as:

$$\tau_{rad} = -J_\infty\ddot{\theta} - \tilde{\tau}_{rad} \tag{3}$$

$$\tilde{\tau}_{rad} = h_r * \dot{\theta} \tag{4}$$

The $*$ operation is the convolution between the impulse response function and the angular velocity $\dot{\theta}$ which can be approximated by a state space model as:

$$\dot{x}_r = A_r x_r + B_r\dot{\theta} \tag{5}$$

$$\tilde{\tau}_{rad} = C_r x_r + D_r\dot{\theta} \tag{6}$$

where A_r, B_r, C_r and D_r are the radiation matrices which are identified from the radiation impulse response function. The excitation torque can be expressed by the convolution between the impulse response function and the wave elevation:

$$\tau_{ex} = h_{ex} * \eta \tag{7}$$

Hence the convolution can also be approximated by a state space model as:

$$\dot{x}_e = A_e x_e + B_e \eta \tag{8}$$
$$\tau_{ex} = C_e x_e \tag{9}$$

where A_e, B_e and C_e are the excitation matrices which are identified from the excitation impulse response function. The parameters of the floater are listed in Table 1 in the appendix.

3. The Hydraulic PTO system

In this paper, the Discrete Displacement Cylinder (DDC) Hydraulic system is used to apply the PTO torque. A simplified illustration for this system is shown in Fig. 3. More details about the DDC hydraulic system can be found in reference [19].

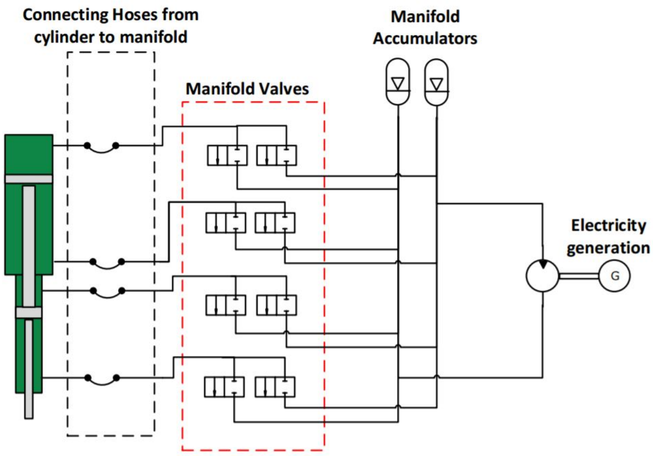

Figure 3. The layout of the DDC hydraulic system

As shown in Fig. 3, the DDC hydraulic system is mainly composed of the actuator/cylinder, the manifold valves, the manifold accumulators, and the generator. The PTO torque is computed as the product of the cylinder force and the moment arm:

$$\tau_{PTO} = F_c l_1 \tag{10}$$

where the moment arm can be expressed as:

$$l_1 = \frac{l_2 l_3 \sin(\theta - \alpha_0)}{x_c + l_4} \tag{11}$$
$$x_c = -l_4 + \sqrt{-2 l_2 l_3 \cos(\theta - \alpha_0) + (l_2^2 + l_3^2)} \tag{12}$$

3.1. The hydraulic cylinder

The actuator force F_c is generated by the hydraulic cylinder and it can be computed as:

$$\tilde{F}_c = -p_{A1} A1 + p_{A2} A2 - p_{A3} A3 + p_{A4} A4 \tag{13}$$
$$F_c = \tilde{F}_c - F_{fric} \tag{14}$$

where p_{Ai} is the pressure of the ith chamber and Ai is the area of the piston. F_{fric} is the cylinder friction force. The dynamics of the chamber pressure can be described by the flow continuity equation:

$$\dot{p}_{A1} = \frac{\beta(p_{A1})}{A1(x_{c,max} - x_c) + V_{0,A1}}(Q_{A1} - v_c A1) \tag{15}$$

$$\dot{p}_{A2} = \frac{\beta(p_{A2})}{A2 x_c + V_{0,A2}}(Q_{A2} + v_c A2) \tag{16}$$

$$\dot{p}_{A3} = \frac{\beta(p_{A3})}{A3(x_{c,max} - x_c) + V_{0,A3}}(Q_{A3} - v_c A3) \tag{17}$$

$$\dot{p}_{A4} = \frac{\beta(p_{A4})}{A4 x_c + V_{0,A4}}(Q_{A4} + v_c A4) \tag{18}$$

where $V_{0,A1}$, $V_{0,A2}$, $V_{0,A3}$ and $V_{0,A4}$ are the volumes of the connecting hoses of different chambers. $x_{c,max}$ is the maximum stroke of the cylinder. x_c and v_c are the position and velocity of the piston respectively which are defined positive down. $\beta(p_{Ai})$ is the effective bulk modulus of the fluid based on different pressure which is assumed to be constant in this study. Additionally, Q_{Ai} is the flow from the connecting hose to ith chamber. The cylinder friction is expressed as:

$$F_{fric} = \begin{cases} \tanh(a v_c) \mid \tilde{F}_c \mid (1 - \eta_c), & \text{if } F_c v_c > 0 \\ \tanh(a v_c) \mid \tilde{F}_c \mid (\frac{1}{\eta_c} - 1) & \text{otherwise} \end{cases} \tag{19}$$

where a is the coefficient used to smooth the friction curve versus velocity. η_c is a constant efficiency of the cylinder.

3.2. The hoses

The hoses connected between the cylinder and the manifold valves are modeled as:

$$\dot{Q}_{out} = \frac{(p_1 - p_2)A_{hose} - p_f(Q_{out})A_{hose}}{\rho l_{hose}} \tag{20}$$

$$\dot{p}_1 = \frac{(Q_{in} - Q_{out})\beta}{A_{hose} l_{hose}} \tag{21}$$

where Q_{in} and Q_{out} are the fluid flows in and out the hose, p_1 and p_2 are the pressures of the inlet and outlet of the hose respectively, A_{hose} is the area of the hose, l_{hose} is the length of the hose, ρ is the fluid density, and $p_f(Q_{out})$ is the pressure drop across the hose. The pressure drop across a straight pipe/hose can be modeled as:

$$\begin{aligned} p_\lambda = {} & \frac{0.3164 l_{hose}\rho}{2Re^{0.25} d_{hose}} \frac{Q_{out} \mid Q_{out} \mid}{(0.25 d_{hose}^2 \pi)^2}(0.5 + 0.5\tanh(\frac{2300 - Re}{100})) \\ & + \frac{128 \nu \rho l_{hose} Q_{out}}{\pi d_{hose}^4}(0.5 + 0.5\tanh(\frac{-2300 + Re}{100})) \end{aligned} \tag{22}$$

where ν is the kinematic viscosity of the fluid. Re represents the Reynold number which can be computed as:

$$Re = \frac{v_{out} d_{hose}}{\nu} \tag{23}$$

Eq. (22) combines the pressure loss of the laminar flow and the turbulent flow by the hyperbolic-tangent expression. Consequently, a continuous transition of the pressure loss between the laminar and turbulent flow can be created. When the Reynold number is less than 2200, $(0.5 + 0.5\tanh(\frac{2300-Re}{100}))$ is close to zero which means the pressure drop is contributed by the laminar flow. On the other hand, when the Reynold number is greater than 2400, $(0.5 + 0.5\tanh(\frac{-2300+Re}{100}))$

is close to zero which means the pressure drop is contributed by the turbulent flow. Another source of pressure drop is the the fitting losses which can be computed as:

$$p_\zeta = \zeta \frac{\rho}{2} Q_{out} \mid Q_{out} \mid \frac{1}{(0.25 d_{hose}^2 \pi)^2} \tag{24}$$

where ζ is the friction coefficient for a given fitting type. Finally, the total resistance in the hose with n line pieces and m fittings can be computed as:

$$p_f(Q_{out}) = p_{\lambda,1}(Q_{out}) + ... + p_{\lambda,n}(Q_{out}) + p_{\zeta,1}(Q_{out}) + ... + p_{\zeta,m}(Q_{out}) \tag{25}$$

In this paper, the pressure loss of the hoses is modeled as:

$$p_f(Q_{out}) = p_\lambda(Q_{out}) + p_{\zeta,M}(Q_{out}) + p_{\zeta,C}(Q_{out}) \tag{26}$$

where $p_{\zeta,M}$ represents the fitting resistance which considers the internal pressure drops in the manifold and $p_{\zeta,C}$ represents the cylinder inlet loss.

3.3. The directional valves

The two-way two-position directional valves are used in this model. The flow across the valve can be described by the orifice equation:

$$Q_v = sign(\Delta p) C_d A_v(\alpha) \sqrt{\frac{2}{\rho} \mid \Delta p \mid} \tag{27}$$

where Δp is the pressure difference cross the valve, C_d is the discharge coefficient and $A_v(\alpha)$ is the opening area which can be computed as:

$$A_v(\alpha) = \alpha A_0 \tag{28}$$

$$\dot{\alpha} = \begin{cases} \frac{1}{t_v}, & \text{if } u_v = 1 \\ -\frac{1}{t_v}, & \text{if } u_v = 0 \end{cases} \tag{29}$$

$$0 \leqslant \alpha \leqslant 1 \tag{30}$$

where A_0 is the maximum opening area of the valve. In this paper, a total of 8 valves are used to control the actuator force.

3.4. The pressure accumulators

The accumulators in the DDC system are used as pressure sources and also for energy storage. The dynamics of the pressure accumulator can be modeled as [19]:

$$\dot{p}_{acc} = \frac{Q_{acc} + \frac{1}{1+\frac{R}{C_v}} \frac{V_g}{T} \frac{1}{\tau_a}(T_w - T)}{\frac{V_{a0} - V_g + V_{ext}}{\beta} + \frac{1}{1+\frac{R}{C_v}} \frac{V_g}{p_{acc}}} \tag{31}$$

$$\dot{V}_g = -Q_{acc} + \dot{p}_{acc} \frac{V_{a0} - V_g + V_{ext}}{\beta} \tag{32}$$

$$\dot{T} = \frac{1}{\tau_a}(T_w - T) - \frac{RT}{C_v V_g} \dot{V}_g \tag{33}$$

where p_{acc} is the pressure of the accumulator, Q_{acc} is the inlet flow to the accumulator, R is the ideal gas constant, C_v is the gas specific heat at constant volume, T_w is the wall temperature, τ_a is the thermal time constant, β is the bulk modulus of the fluid in the pipeline volume V_{ext}, V_{a0} is the size of the accumulator, V_g is the gas volume, and T is the gas temperature. Hence the state of the accumulator contains the pressure, the gas volume and the gas temperature. Initially, the state can be specified based on the standard gas law:

$$V_g = \frac{T}{T_0} \frac{p_{a0}}{p_a} V_{a0} \tag{34}$$

where p_{a0} is the pre-charged pressure of the gas at the temperature T_0.

3.5. The hydraulic motor

For the system presented in this paper, there are 4 chambers and 2 different pressures: the high pressure and the low pressure. The hydraulic motor is connected between the high pressure accumulator and the low pressure accumulator. The flow of the hydraulic motor can be modeled as:

$$Q_M = D_w \omega_M - \Delta p C_{Q1} \tag{35}$$

where D_w is the displacement of the hydraulic motor, which is constant for a fixed displacement motor, Δp is the pressure across the motor, C_{Q1} is the coefficient of the flow loss of the motor, and ω_M is the rotational speed of the motor which is defined as:

$$\omega_M = \frac{p_{avg,exp} \psi}{p_H k_{gen} D_M} \tag{36}$$

where $p_{avg,exp}$ is the expected average power output, p_H is the pressure of the high pressure accumulator, k_{gen} is the number of generators, D_M is the total motor displacement, and ψ is a coefficient for the motor speed control to prevent the high pressure from depletion or saturation which is formulated as:

$$k = \frac{4}{(p_{H,max} - p_{H,min})} \tag{37}$$

$$\psi = \begin{cases} k(p_H - p_{H,min}), & \text{if } p_H > p_{H,min} \\ 0, & \text{otherwise} \end{cases} \tag{38}$$

To achieve the desired motor speed introduced in Eq. (36), the generator torque control need to be included. In this paper, the generator and inverter are not modeled and the desired motor speed is assumed achievable. The power in the hydraulic motor can be computed as:

$$P_M = \Delta p Q_M \tag{39}$$

This completes the modeling of DDC hydraulic system; the control algorithm is introduced in the next section.

4. The control algorithm

Two parts will be presented in this section: the control method for the buoy and the force shifting algorithm for controlling the valves. The control method for controlling the buoy computes a reference value for the control force at each time step. This reference control force is then used as an input to the PTO, and the actual control force that results from the PTO is computed using the force shifting algorithm. Each of the two parts is detailed below.

4.1. The buoy control method

Several control methods will be tested in this paper using a simulator that simulates the PTO unit. Some of these controller were originally developed for heave control. It is relatively straightforward, however, to extend a control method from the heave motion to the pitch motion. For example, the Singular Arc (SA) control method [29] can be used to compute the control torque as follows:

$$\tau_{PTO}(s) = \frac{N(s)}{D(s)} \tag{40}$$

where:

$$\begin{aligned} N(s) &= (J_{total}s^2 + (C_r(sI + A_r)^{-1}B_r - D_r)s \\ &\quad + K_{res})\tau_{ex}(s) \\ D(s) &= s(C_r(sI + A_r)^{-1}B_r - C_r(sI - A_r)^{-1}B_r \\ &\quad - 2D_r) \end{aligned} \tag{41}$$

where the excitation torque can be expressed as Fourier Series expansion:

$$\tau_{ex} = \sum_{i=1}^{n} \Re(\tau_{c,ex}(\omega_i)\eta(\omega_i)e^{i(-\omega_i t + \phi_i)}) \tag{42}$$

An inverse Laplace transformation is then applied to the SA control to obtain the control in the time domain. The required information to compute the control is the time t, the excitation torque coefficient $\tau_{c,ex}$, the wave frequency vector $\vec{\omega}$ and the time domain phase shift vector $\vec{\phi}$.

A reference control method is the feedback Proportional-Derivative (PD) control. The PD control takes the form:

$$\tau_{PTO} = K\theta + B\dot{\theta} \tag{43}$$

where K is the proportional gain and B is the derivative gain.

In addition to the above two control methods, simulated in this paper are the Model Predictive Control (MPC) [30], the shape-based (SB) control [31], a proportional-derivative complex conjugate control (PDC3) [32], and the pseudo-spectral control (PS) [33]. Each one of these methods is well documented in the literature, so the details of each control methods is avoided in this paper.

In the original developments, the SA control and the PDC3 control compute a control force that is equivalent to the complex conjugate control (C3) and hence the maximum possible harvested energy in the linear domain. However, the C3 does not account for constraints on the buoy displacement. In fact, since the C3 criteria is to resonate the buoy with the excitation force, the motion of the buoy always violates displacement constraints when controlled using the SA and PDC3 controls. On the other hand, the MPC, SB, and PS control methods compute a control force, in an optimal sense, taking displacement constraints into account. Figure 4 shows a simulation for 5 minutes for the above six control methods when a constraint on the buoy displacement is assumed. The simulation parameters are detailed in Section 5. This simulation does not account for the PTO dynamics and it is here presented to highlight the impact of including the PTO in the simulations in Section 5. As can be seen from Figure 4, among the six control methods, the MPC and PD controls performed best, then the SB method, then the PS, and then the PDC3 and SA methods. The two methods (SA and PDC3) that perform best without displacement constraints actually perform the least when accounting for the constraints.

4.2. The force shifting algorithm

The force shifting algorithm (FSA) is introduced in this section. The FSA used in this paper has the following algorithm:

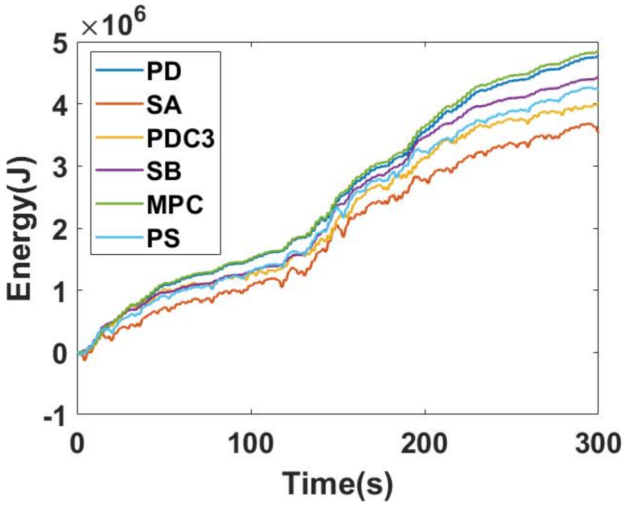

Figure 4. When accounting for displacement constraints, some unconstrained methods harvest less energy

$$\{F_c(t) = \vec{F}[k] \mid k = arg\ \ min \mid F_{ref}(t) - \vec{F}[k] \mid\} \tag{44}$$

where F_{ref} is the reference control force (computed for instance using one of the six control methods described above), $\vec{F}$ is the vector of the possible discrete values for the force. With different permutations of valves openings, it is possible to produce different levels of constant forces as shown in Fig. 5, where it is assumed here that $p_H = 200$ bar and $p_L = 20$ bar. The FSA selects the discrete force level that is closest to the reference control force. It is noted here that the discrete force changes over time due to the fluctuation of the pressures in the accumulators.

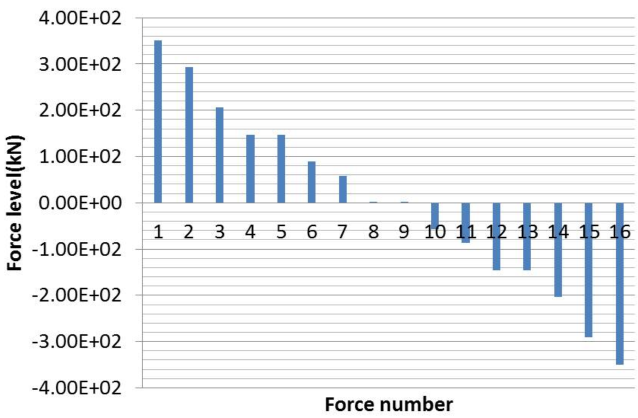

Figure 5. An example for all discrete possible values for a PTO force

5. Simulation Tool

A tool for simulating the dynamics of the WEC including the motion dynamics, the hydrodynamics/hydrostatic forces calculations, and the PTO hardware model was developed in MathWorks Simulink®. The detailed Simulink model of the wave energy conversion system is shown in Fig. 6. The Plant block simulates the dynamics of the buoy. The PTO block simulates all the equations of the valves, hoses, and accumulators. The Decoder and 'Discrete F ref' blocks simulate the discrete force shifting algorithm. As can be seen in the figure, the excitation force is an input that is

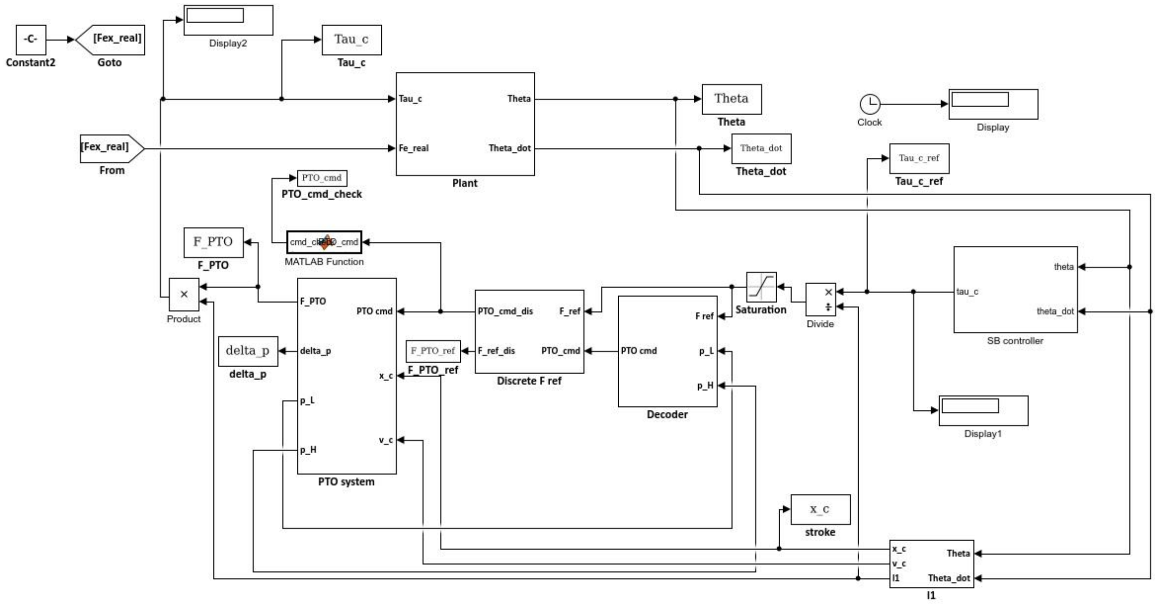

Figure 6. The Simulink model of the wave energy conversion system

computed outside the Plant block. The control force is computed in the block 'SB controller'. Despite the name, six different controllers were tested in the 'SB controller' block. The detailed Simulink model of the hydraulic system is shown in Fig. 7, this model is inside the PTO block in Fig. 6.

The parameters of the dynamic model of the wavestar used in the simulations in this paper are listed in Table 1.

Table 1. Model parameters for the Wavestar

Symbol	Value	Unit
J_{tot}	3.8×10^6	kg m^2
K_{res}	14×10^6	Nm/rad
The transfer function $H_r(s)$		
$(b_0, b_1, ..., b_5)$	*	
$(a_0, a_1, ..., a_5)$	**	
The transfer function $H_{ex}(s)$		
(b_0, b_1)	***	
$(a_0, a_1, ..., a_4)$	****	

* = $(0.0001, 0.0144, 0.624, 8.16, 13.1, 1.44) \times 10^6$
** = $(0.001, 0.0906, 1.67, 6.31, 13.3, 9.18)$
*** = $(5.4, 270) \times 10^4$
**** = $(0.036, 0.39, 1.5, 2.6, 1.6)$

5.1. Wave model

Irregular waves are simulated in this study using the stochastic Pierson-Moskowitz Spectrum. The spectral density is defined as:

$$S(\omega) = \frac{5H_{m0}^2}{\omega_p \omega_n^5} e^{-\frac{5}{4\omega_n^4}} \tag{45}$$

where $\omega_n = \omega/\omega_p$, ω_p is the peak frequency and H_{m0} is the significant height of the wave. The wave used in the simulation has a significant height of 1.75 m and a peak period 5.57 s.

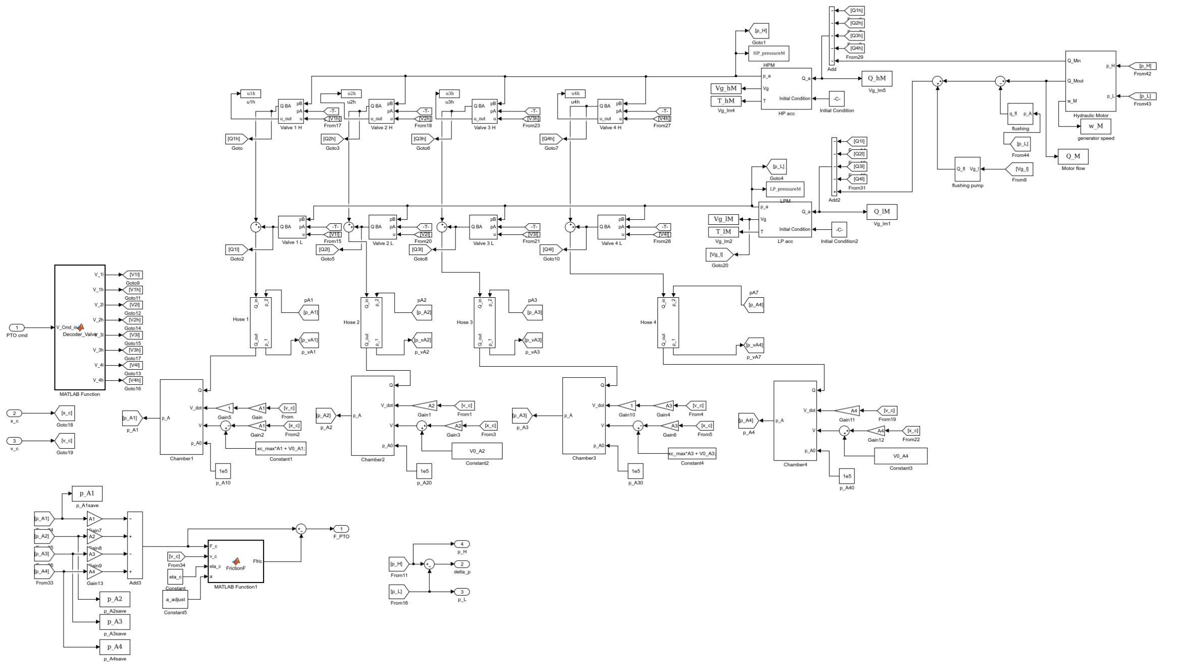

Figure 7. The Simulink model of the hydraulic PTO system

5.2. The system losses

The system losses are computed in this study. The system losses include the pressure loss of the hoses, the flow loss of the generator and the friction of the cylinder. The pressure loss is shown in Fig. 8, in which the vertical line represents the transition between the laminar flow and the turbulent flow when the Reynold number is $Re = 2300$, for each of the two possible directions of the fluid flow. The amount of the flow loss and the friction force of the cylinder are shown in Fig. 9 and Fig. 10. All the system parameters used in the simulations in this paper are listed in Table 2.

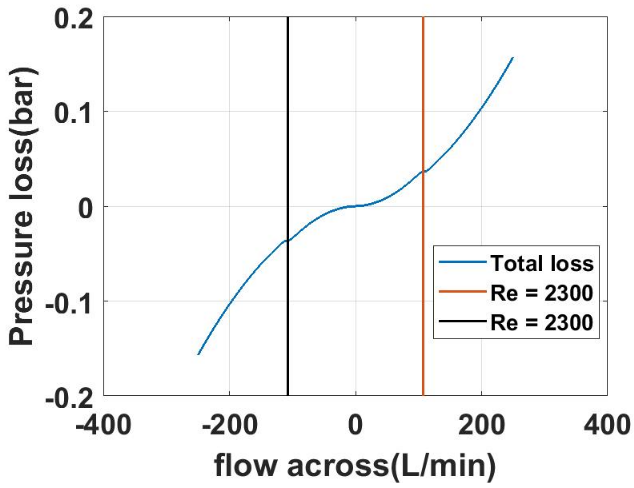

Figure 8. The pressure loss of the hose which has 1m length and 3.81×10^{-2}m diameter with different flow rate across the hose.

Table 2. The data used in the simulation of overall WEC system

Symbol	Value	Unit
Length of the arms		
l_2	3	m
l_3	2.6	m
l_4	1.6	m
Length of the hoses C2M		
l_{A1}	1	m
l_{A2}	1	m
l_{A3}	1	m
l_{A4}	1	m
Diameter of the hoses C2M		
d_{A1}	1.5	in
d_{A2}	1.5	in
d_{A3}	1.5	in
d_{A4}	1.5	in
Maximum stroke		
$x_{c,max}$	3	m
Area of the chambers		
A_1	113.4×10^{-4}	m^2
A_2	32.55×10^{-4}	m^2
A_3	80.85×10^{-4}	m^2
A_4	162.75×10^{-4}	m^2
Max Area of the valves		
A_{01}	1.6×10^{-4}	m^2
A_{02}	1.6×10^{-4}	m^2
A_{03}	1.6×10^{-4}	m^2
A_{04}	1.6×10^{-4}	m^2
Accumulator size		
V_{a0}	100×10^{-3}	m^3
Pressure drop coef		
ζ_M	1.3	
ζ_C	1	
Specific time constant S		
τ_l	23	s
τ_h	34	s
Initial Pressure of the accumulators		
$p_{a,l}$	20	bar
$p_{a,h}$	130	bar
Initial angle		
α_0	1.0821	rad
Control parameters		
K	-9.16×10^6	Nm/rad
B	4.4×10^6	Nms/rad
Valve opening time		
t_v	30×10^{-3}	s
Wall temperature		
T_w	50	^oC
Ideal gas constant		
R	276	J/kg/K
Gas specific heat at constant volume		
C_v	760	J/kg/K
Motor displacement		
D_w	100	cc/rev
Flow loss coefficient		
C_{Q1}	5.4×10^{-12}	$m^3/s/Pa$
Fluid bulk modulus		
β	1.5×10^9	Pa

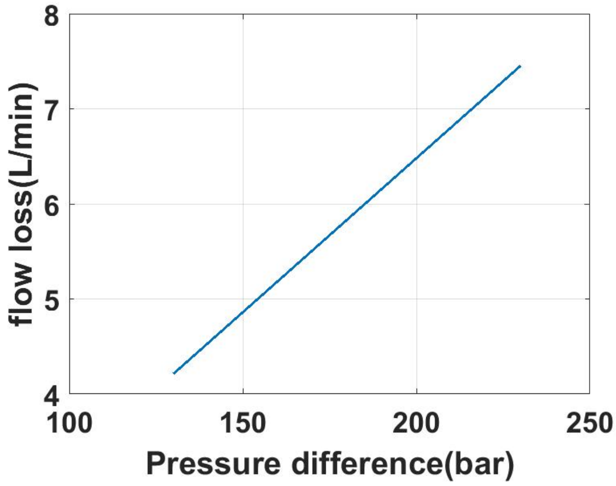

Figure 9. The flow loss of the generator

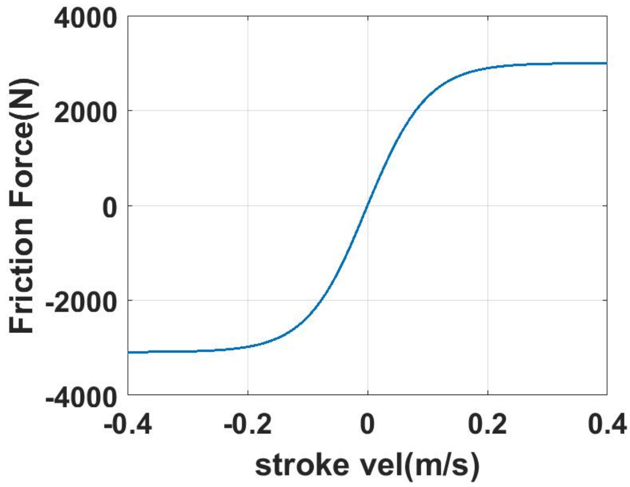

Figure 10. The friction force of the cylinder with different velocities when the cylinder force is 100 kN.

6. Simulation Results

The above Simulink tool is used to simulate the performance of the above six control methods. The energy extracted by method is shown in Fig. 11. In this simulation, there is limitations on the maximum stroke and the maximum control force. In addition, the PTO dynamics are simulated. The maximum control force in the cylinder in the simulations presented in this paper is assumed to be 215 kN. The maximum allowable displacement in the simulations presented in this paper is assumed to be 1.2 m. As can be shown in Fig. 11, the MPC and PD control methods harvest the highest energy level compared to the other methods. The SB method comes next. The SA, PDC3, and the PS control methods come next, and the three of them perform about the same. Comparing Fig. 11 to Fig. 4 we can see that by including the PTO model, the performance of the SA method improved slightly while the performance of the PS degraded slightly and as a result the three methods PS, SA, and PDC3 perform about the same. The performance of the MPC, PD, and SB control methods actually slightly improved when the PTO model is included.

Another important result to examine is the output mechanical power at the actuator and the output power from the generator. These two quantities are compared in Fig. 12. From the figure we can tell that the power absorbed in the generator side is much smoother than the power extracted

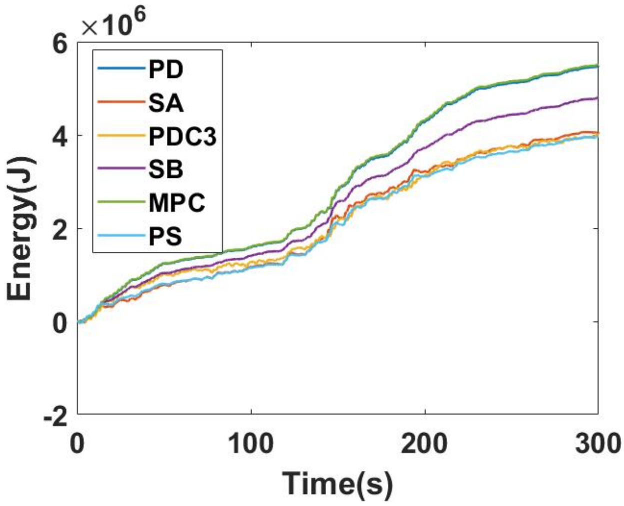

Figure 11. The energy extracted accounting for displacement and force constraints and including the hydraulic system dynamics model

by actuator. The hydraulic accumulators act as power capacitor for energy storage resulting in this relatively smooth power profile at the generator output. As can be seen in the figure also, the actuator power includes reactive power; these are the times at which the actuator power is negative. At these times, the PTO actually pumps power into the ocean through the actuator. The generator output power does not have any reactive power confirming that all the reactive power come from the accumulators.

The efficiency of the system is defined as:

$$\eta_c = \frac{P_{gen}}{P_{actuator}} \tag{46}$$

The efficiency depends on the control method. For example, in this test case, the efficiency of the SB controller is 80.15%, for the MPC it is 72.58%, for the PS it is 67.34%, for the SA it is 64.36%, and for the PD controller it is 71.76%, over 300 seconds.

In the context of comparing the performance of different control methods, it is important to highlight one significant difference between them that emanates from the theory behind each control method. Each of the MPC, SB and PS control methods requires wave prediction; that is wave information (or excitation force) is needed over a future horizon at each time step in the simulation. In the simulations in this paper, this future horizon is assumed to be 0.6 seconds for the SB and MPC control methods, and is assumed to be 60 seconds for the PS control. Wave prediction is assumed perfect in these simulations. Non-perfect wave prediction would affect the results obtained using these methods. The PD, SA, and PDC3 control methods do not need future wave prediction.

This simulation tool also provides detailed operation information that are useful to characterize different components in the system. For example, the generator speed is computed in the simulation, and is shown in Fig. 13. As shown in the figure, the speed is oscillating around 1200 RPM.

To present detailed plots for the response of the buoy, only one control method is selected as a sample to avoid excessive number of figures in the paper. The SB method is selected here to present the detailed WEC response in this section. The angular displacement of the buoy is shown in Fig. 14; the maximum angular displacement is about 10 degrees and it is below 5 degrees most of the time. The angular velocity of the buoy is shown in Fig. 15. The cylinder force and the PTO torque are shown in Fig. 16 and 17, respectively. Both the reference and actual values are plotted in each of the two figures. As can be seen in Fig. 16, the control force is below the force limit of 215 kN. The accumulator pressure is shown in Fig. 18. The high pressure is oscillating around 100 bar, while the low pressure is stable around 20 bar. The chamber pressure is shown in Fig. 19. Significant fluctuations can be observed when the hydraulic system is extracting energy. This is necessary to be able to track the reference control command effectively. Yet, those fluctuations may be reduced by increasing the valve opening area or including relief valves.

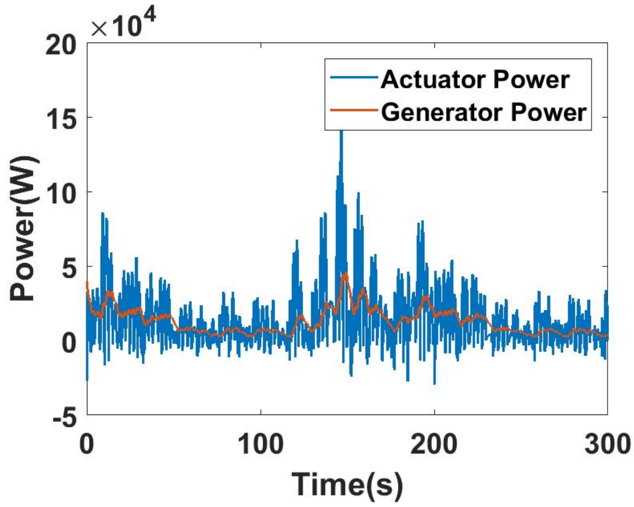

Figure 12. The Power extracted by the actuator and the generator

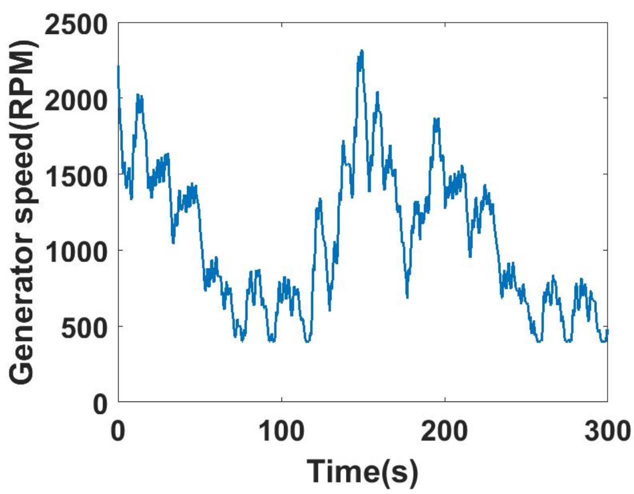

Figure 13. The generator speed

7. Discussion

In this paper, different recent control methods are tested using a simulation tool that simulates a hydraulic PTO system. In a theoretical test (where PTO is assumed to track reference control command ideally and in the absence of all constraints,) the SA controller has the best performance in terms of energy extraction. Yet the performance of the SA controller with the hydraulic system model included is the worst among the tested six control methods. To get more insight into this phenomenon, consider Table. 3 that presents data for three controllers (SA, PD, and PDC3) in the theoretical test case. As can be seen in Table. 3, the energy extracted by the PD controller in this theoretical test is about 60% of that of the SA controller. However, the buoy maximum displacement associated with the SA control is significantly higher than that of the PD control (almost three times higher) which makes it more difficult to achieve. Similarly, the maximum control force required by

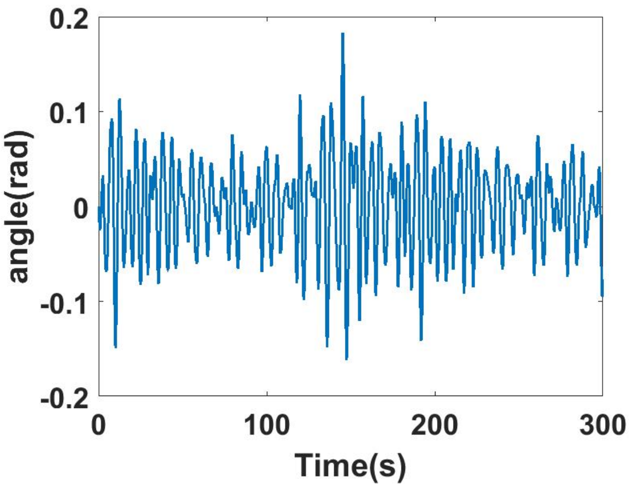

Figure 14. The rotational angle

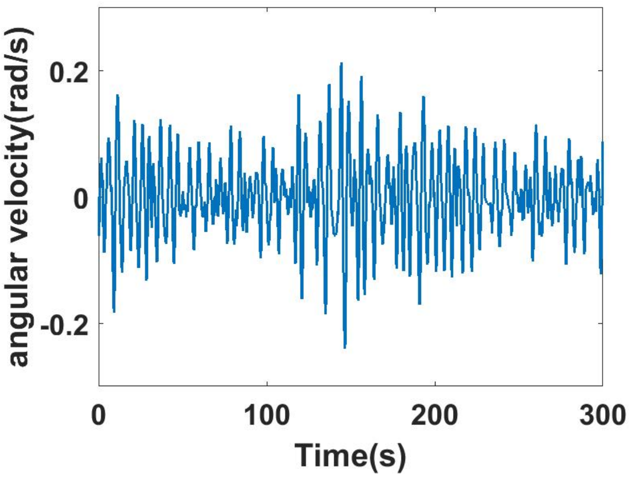

Figure 15. The angular velocity

the SA control is significantly higher than that of the PD control which means a PTO might not be able to track the command force at all times when using a SA control, while it is more likely to track a command force generated using a PD control. The data of the PDC3 control in Table. 3 also highlights that the PDC3 control in this test case generates about the same level of average power; yet at higher displacement range and higher force capability. This indicates that including a model for the PTO would result in favorable performance for the PD control compared to the PDC3. To highlight the impact of the PTO model on the performance of the different control strategies, consider Table. 4. The data are presented for all the six control methods. As can be seen from Table. 4, all the control methods reached the maximum possible control capacity allowable by the PTO. Since this maximum control force is well below that needed by the SA in Table. 3, the amount of harvested energy in this practical case is significantly less than the one computed in the theoretical case (13.49 W compared to 35.11 W in average power). The drop in energy harvested using the PD control however is less since the maximum force needed theoretically was as high as that of the SA. The displacement of the PDC3 reached the maximum displacement allowable by the WEC (1.2 m.) This is expected since the PDC3 tends to increase the displacement and hence it would reach a limit imposed by the WEC system.

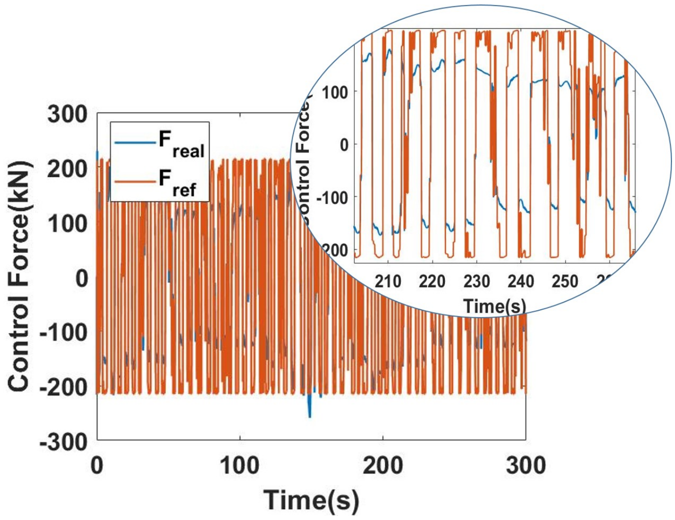

Figure 16. The cylinder force

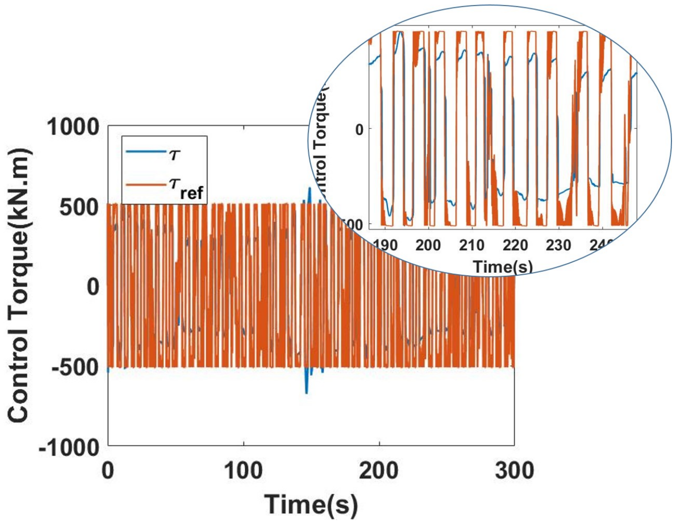

Figure 17. The PTO torque

Table 3. Capacity requirement of the controllers without hydraulic system

Symbol	Value	Unit
The SA controller		
$F_{PTO,max}$	3705	kN
$x_{c,max} - x_{c,min}$	3.2	m
P_{ave}	35.11	W
The PD controller		
$F_{PTO,max}$	1119	kN
$x_{c,max} - x_{c,min}$	1.1	m
P_{ave}	21.00	W
The PDC3 controller		
$F_{PTO,max}$	1404	kN
$x_{c,max} - x_{c,min}$	1.6	m
P_{ave}	21.08	W

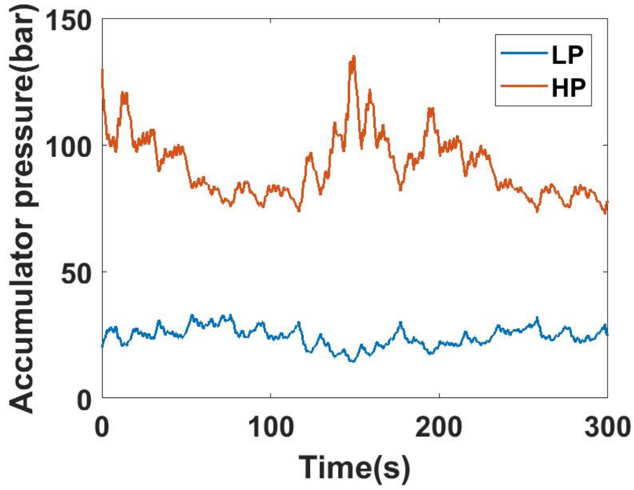

Figure 18. The pressure of the accumulator

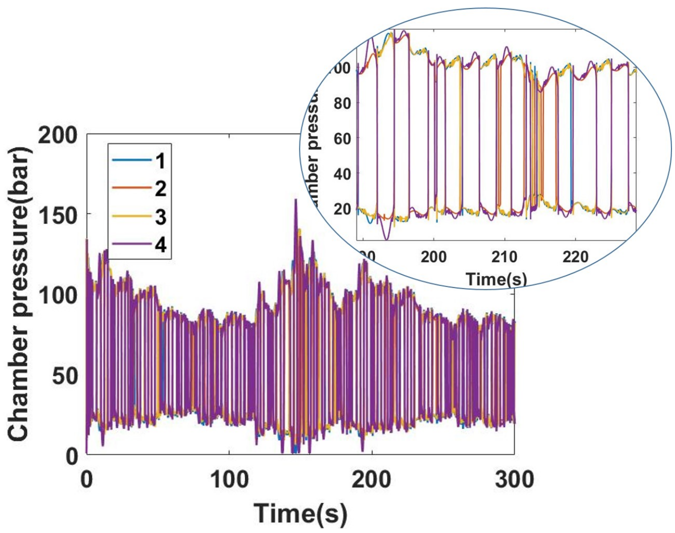

Figure 19. The chamber pressure

8. Conclusion

The main conclusion of this paper is that a controller that is optimal in a theoretical analysis might not be optimal when tested in a practical test environment. In particular, this paper sheds light on considerations that need to be accounted for in designing a control method for WEC systems. The first of these considerations is the limitation of the maximum possible PTO control force. This limitation impacts methods such as the singular arc control which is a control method developed in an optimal sense using classical optimal control theory. The second consideration is the limitation due to the maximum possible displacement of the WEC system. This limitation impacts the optimality of some control methods such as the multi-resonant proportional derivative control that is derived in an optimal sense to satisfy the complex conjugate criterion. Another consideration is the capability of the PTO to track the control command. The hydraulic PTO presented in this paper produces discrete levels of control forces and hence the dynamics of this PTO need to be accounted for in designing a control system for practical energy harvesting.

Acknowledgments: This material is based upon work supported by the National Science Foundation under Grant Number 1635362.

Table 4. Capacity requirement of the controllers with hydraulic system

Symbol	Value	Unit
The SA controller		
$F_{PTO,max}$	215	kN
$x_{c,max} - x_{c,min}$	0.96	m
P_{ave}	13.49	W
The PD controller		
$F_{PTO,max}$	215	kN
$x_{c,max} - x_{c,min}$	1.1	m
P_{ave}	18.26	W
The PDC3 controller		
$F_{PTO,max}$	215	kN
$x_{c,max} - x_{c,min}$	1.2	m
P_{ave}	13.32	W
The SB controller		
$F_{PTO,max}$	215	kN
$x_{c,max} - x_{c,min}$	0.8	m
P_{ave}	16.02	W
The MPC controller		
$F_{PTO,max}$	215	kN
$x_{c,max} - x_{c,min}$	1.1	m
P_{ave}	18.37	W
The PS controller		
$F_{PTO,max}$	215	kN
$x_{c,max} - x_{c,min}$	0.90	m
P_{ave}	13.22	W

Author Contributions: Shangyan Zou and Ossama Abdelkhalik designed the study and analyzed the data. Shangyan Zou wrote the paper and Ossama Abdelkhalik revised the paper.

Conflicts of Interest: The authors declare no conflict of interest.

Bibliography

1. António, F.d.O.; Justino, P.A.; Henriques, J.C.; André, J.M. Reactive versus latching phase control of a two-body heaving wave energy converter. Control Conference (ECC), 2009 European. IEEE, 2009, pp. 3731–3736.
2. Bacelli, G.; Ringwood, J.V.; Gilloteaux, J.C. A control system for a self-reacting point absorber wave energy converter subject to constraints. *IFAC Proceedings Volumes* **2011**, *44*, 11387–11392.
3. Ricci, P.; Lopez, J.; Santos, M.; Ruiz-Minguela, P.; Villate, J.; Salcedo, F.; others. Control strategies for a wave energy converter connected to a hydraulic power take-off. *IET renewable power generation* **2011**, *5*, 234–244.
4. You-Guan, Y.; Guo-fang, G.; Guo-Liang, H. Simulation technique of AMESim and its application in hydraulic system [J]. *Hydraulics Pneumatics & Seals* **2005**, *3*, 28–31.
5. Ferri, F.; Kracht, P. Implementation of a Hydraulic Power Take-Off for wave energy applications. *Recuperado de http://www. sdwed. civil. aau. dk/digitalAssets/97/97533_d4* **2013**, *7*.
6. Plummer, A.; Cargo, C. Power Transmissions for Wave Energy Converters: a Review. 8th International Fluid Power Conference (IFK). University of Bath, 2012.
7. Antonio, F.d.O. Modelling and control of oscillating-body wave energy converters with hydraulic power take-off and gas accumulator. *Ocean engineering* **2007**, *34*, 2021–2032.
8. António, F.d.O. Phase control through load control of oscillating-body wave energy converters with hydraulic PTO system. *Ocean Engineering* **2008**, *35*, 358–366.
9. Hansen, R.H. *Design and control of the powertake-off system for a wave energy converter with multiple absorbers*; Videnbasen for Aalborg UniversitetVBN, Aalborg UniversitetAalborg University, Det Teknisk-Naturvidenskabelige FakultetThe Faculty of Engineering and Science.

10. Babarit, A.; Guglielmi, M.; Clément, A.H. Declutching control of a wave energy converter. *Ocean Engineering* **2009**, *36*, 1015–1024.
11. Eidsmoen, H. Tight-moored amplitude-limited heaving-buoy wave-energy converter with phase control. *Applied Ocean Research* **1998**, *20*, 157–161.
12. Eidsmoen, H. Simulation of a slack-moored heaving-buoy wave-energy converter with phase control **1996**.
13. Josset, C.; Babarit, A.; Clément, A. A wave-to-wire model of the SEAREV wave energy converter. *Proceedings of the institution of mechanical engineers, Part M: Journal of Engineering for the Maritime Environment* **2007**, *221*, 81–93.
14. Henderson, R. Design, simulation, and testing of a novel hydraulic power take-off system for the Pelamis wave energy converter. *Renewable energy* **2006**, *31*, 271–283.
15. Zhang, D.; Li, W.; Ying, Y.; Zhao, H.; Lin, Y.; Bao, J. Wave energy converter of inverse pendulum with double action power take off. *Proceedings of the Institution of Mechanical Engineers, Part C: Journal of Mechanical Engineering Science* **2013**, *227*, 2416–2427.
16. Antolín-Urbaneja, J.C.; Cortés, A.; Cabanes, I.; Estensoro, P.; Lasa, J.; Marcos, M. Modeling innovative power take-off based on double-acting hydraulic cylinders array for wave energy conversion. *Energies* **2015**, *8*, 2230–2267.
17. Cargo, C.; Hillis, A.; Plummer, A. Optimisation and control of a hydraulic power take-off unit for a wave energy converter in irregular waves. *Proceedings of the Institution of Mechanical Engineers, Part A: Journal of Power and Energy* **2014**, *228*, 462–479.
18. Sun, K.; Ge, W.; Luo, L.; Liang, H.; Xu, C.; Leng, J.; Yuan, Z.; Huang, H. Research on the hydraulic power take-off unit of a hybrid wave energy converter. OCEANS 2016-Shanghai. IEEE, 2016, pp. 1–4.
19. Hansen, R.H.; Kramer, M.M.; Vidal, E. Discrete displacement hydraulic power take-off system for the wavestar wave energy converter. *Energies* **2013**, *6*, 4001–4044.
20. Hansen, R.H.; Andersen, T.O.; Pedersen, H.C. Model based design of efficient power take-off systems for wave energy converters. 12th Scandinavian International Conference on Fluid Power, SICFP 2011. Tampere University Press, 2011, pp. 35–49.
21. Kamizuru, Y. *Development of hydrostatic drive trains for wave energy converters*; Shaker, 2014.
22. Hals, J.; Taghipour, R.; Moan, T. Dynamics of a force-compensated two-body wave energy converter in heave with hydraulic power take-off subject to phase control. Proceedings of the 7th European Wave and Tidal Energy Conference, Porto, Portugal, 2007, pp. 11–14.
23. Costello, R.; Ringwood, J.; Weber, J. Comparison of two alternative hydraulic PTO concepts for wave energy conversion. Proceedings of the 9th European wave and tidal energy conference (EWTEC). School of Civil Engineering and the Environment, University of Southampton, 2011.
24. Kamizuru, Y.; Liermann, M.; Murrenhoff, H. Simulation of an ocean wave energy converter using hydraulic transmission.
25. Penalba, M.; Sell, N.P.; Hillis, A.J.; Ringwood, J.V. Validating a wave-to-wire model for a wave energy converter—Part I: The Hydraulic Transmission System. *Energies* **2017**, *10*, 977.
26. Schlemmer, K.; Fuchshumer, F.; Böhmer, N.; Costello, R.; Villegas, C. Design and control of a hydraulic power take-off for an axi-symmetric heaving point absorber. Proceedings of the Nineth European Wave and Tidal Energy Conference, Southampton, 2011.
27. Gaspar, J.F.; Calvário, M.; Kamarlouei, M.; Soares, C.G. Power take-off concept for wave energy converters based on oil-hydraulic transformer units. *Renewable Energy* **2016**, *86*, 1232–1246.
28. Sánchez, E.V.; Hansen, R.H.; Kramer, M.M. Control performance assessment and design of optimal control to harvest ocean energy. *IEEE Journal of Oceanic Engineering* **2015**, *40*, 15–26.
29. Zou, S.; Abdelkhalik, O.; Robinett, R.; Bacelli, G.; Wilson, D. Optimal control of wave energy converters. *Renewable Energy* **2017**, *103*, 217–225.
30. Hals, J.; Falnes, J.; Moan, T. Constrained Optimal Control of a Heaving Buoy Wave-Energy Converter. *Journal of Offshore Mechanics and Arctic Engineering* **2011**, *133*, 1–15.
31. Abdelkhalik, O.; Robinett, R.; Zou, S.; Bacelli, G.; Coe, R.; Bull, D.; Wilson, D.; Korde, U. On the control design of wave energy converters with wave prediction. *Journal of Ocean Engineering and Marine Energy* **2016**, *2*, 473–483.

32. Song, J.; Abdelkhalik, O.; Robinett, R.; Bacelli, G.; Wilson, D.; Korde, U. Multi-resonant feedback control of heave wave energy converters. *Ocean Engineering* **2016**, *127*, 269 – 278.
33. Herber, D.R.; Allison, J.T. Wave energy extraction maximization in irregular ocean waves using pseudospectral methods. ASME 2013 International Design Engineering Technical Conferences and Computers and Information in Engineering Conference. American Society of Mechanical Engineers, 2013, pp. V03AT03A018–V03AT03A018.